

# **Multidimensional Modelling of Cross-Beam Energy Transfer for Direct-Drive Inertial Confinement Fusion**

(Hopefully soon to be Dr.) Philip W. X. Moloney

**IMPERIAL**

June 2024

Submitted in partial fulfilment of the requirements for the degree of  
Doctor of Philosophy of Imperial College London

Department of Physics  
Imperial College London  
Prince Consort Road  
London SW7 2AZ



# List of Acronyms

**Rad-MHD** Radiative-Magnetohydrodynamics

**MHD** Magnetohydrodynamics

**Rad-Hydro** Radiative-Hydrodynamics

**LPIs** Laser-Plasma Instabilities

**CBET** Cross-Beam Energy Transfer

**ICF** Inertial Confinement Fusion

**SBS** Stimulated Brillouin Scattering

**TPD** Two Plasmon Decay

**EPW** Electron Plasma Wave

**LLNL** Lawrence Livermore National Laboratory

**IAW** Ion Acoustic Wave

**EPW** Electron Plasma Wave

**NIF** National Ignition Facility

**MIT** Massachusetts Institute of Technology



# 1 Simulations of Cross-Beam Energy Transfer for Magnetised Direct-Drive

This chapter describes a set of simulations which were conducted to understand the role of Cross-Beam Energy Transfer (CBET) in magnetised, direct-drive implosions. Magnetised Inertial Confinement Fusion (ICF) is a promising route to achieving higher target gains, due to the reduction of thermal energy loss at stagnation and additional confinement of the alpha particles responsible for burn propagation. For direct-drive implosions, magnetisation can significantly alter the coronal plasma conditions, due to the introduced anisotropy of thermal transport. The Ion Acoustic Wave (IAW) dispersion relation, which mediates CBET interactions, depends upon the background plasma and therefore significantly altered temperature and density profiles could alter the action of CBET. Before the development of SOLAS, no direct-drive suitable CBET model existed, which was integrated into a Radiative-Magnetohydrodynamics (Rad-MHD) code. Therefore, the CHIMERA-SOLAS framework has enabled the effect of magnetisation on CBET to be studied for a direct-drive implosion.

The chapter begins with a review of experimental and computational work on magnetised ICF, with a particular focus on magnetised direct-drive. Work presented in this chapter focuses on the study of *exploding-pusher* experiments. These are very different implosions to the typical *central hot-spot* ignition designs, presented in previous chapters, so a short summary of exploding pushers is also provided. Simulation results are presented of 1-D and 2-D, unmagnetised exploding pushers, both with and without the effect of CBET, which demonstrate that CBET does significantly alter these implosions. This is followed by an investigation of how various extended-Magnetohydrodynamics (MHD) terms affect the implosion, including the Nernst effect, the Lorentz force and resistive diffusion of the magnetic field. Results are given of how magnetisation affects the CBET interaction and ultimately how it changes the stagnation shape of the target. The results presented, demonstrate that redistribution of deposited power due to CBET reduced the amplitude of the stagnation asymmetry, which originated from the polar beam configuration used. However, the reduction of asymmetry was consistent for different initial seed magnetic field values, and therefore CBET was not observed to be sufficiently strongly affected by magnetisation, to lead to observable signatures in experimental measurements. The chapter concludes with a summary of the work and suggestions of additional experimental configurations, which may leave a more significant signature of magnetisation altering CBET.

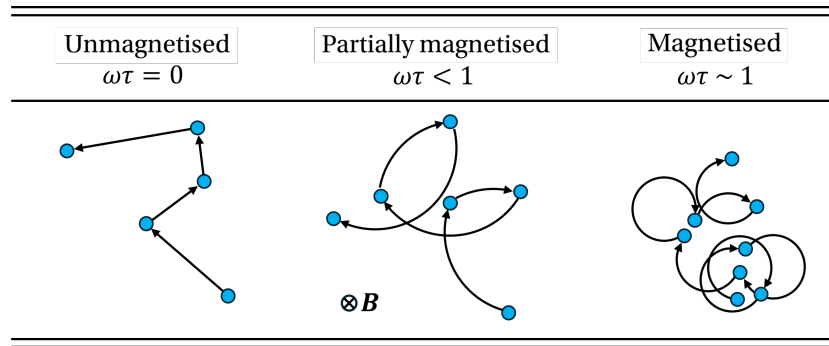


Figure 1.1: Cartoon to illustrate the effect of magnetisation on collisions, and therefore transport, of a test positive charge. Particle locations after collision are represented as blue circles and the path taken by the particle is shown by the black arrows. As the Hall parameter of the particle increases, diffusion is increasingly limited, and therefore collision transport is reduced.

## 1.1 Magnetised Inertial Confinement Fusion and Exploding Pushers

This chapter begins with a review of published studies of relevance to the work conducted in this chapter. Firstly, a short review of magnetised-ICF is presented, which reviews both the key concepts, existing studies and potential challenges of the design. Both work on direct- and indirect drive is summarised, alongside recent theoretical progress on understanding how magnetisation can effect Laser-Plasma Instabilities (LPIs). The exploding pusher concept is then briefly explored to aid understanding of the implosion physics, which is markedly different to conventional hot-spot ICF.

### 1.1.1 Potential Benefits of Target Magnetisation

Magnetisation of an ICF target has long been thought of as a potential aid to ignition [1, 2]. It is still a relevant field of study in the context of regular ignition events on the National Ignition Facility (NIF), because by relaxing the ignition threshold, magnetisation could make larger targets feasible at equivalent laser energy, and therefore lead to higher gains than unmagnetised implosions. For a central hotspot ignition targets, ignition occurs when the heat source of alpha energy deposition balances the thermal and radiative losses in the hotspot. Thermal conduction is suppressed perpendicular to magnetic field lines, therefore a magnetic field can reduce thermal losses and aid the power balance required for ignition. Fig. 1.1 demonstrates the effect of increasing magnetisation on a unit positive test charge. By constraining charged particles to orbit field lines, collisional transport terms, such as thermal conduction, are reduced perpendicular to the field direction. Fits of transport coefficients to Fokker-Planck simulations, demonstrate that in a Hydrogen plasma, thermal conductivity perpendicular to field lines  $\kappa_{\perp}$ , is reduced to  $\sim 30\%$  of the parallel value  $\kappa_{\parallel}$  at Hall parameter  $\omega\tau = 1$ , and  $\sim 1\%$  at  $\omega\tau = 10$  [3]. Thus, for Hall parameters,  $\omega\tau \gtrsim 10$ , thermal conduction losses are almost negligible in the direction perpendicular to field lines.

Using an order of magnitude estimate for a below ignition threshold hotspot,  $T_e \sim 2.5$  keV

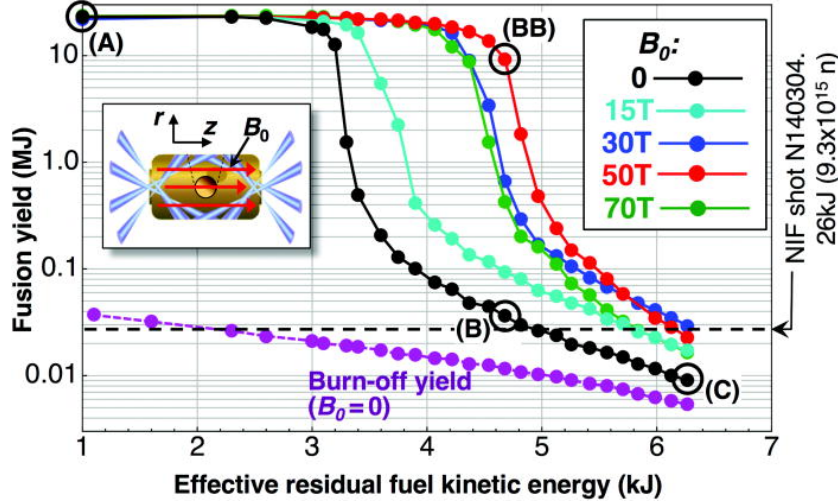


Figure 1.2: Simulated fusion yields versus effective residual fuel kinetic energy under imposed low-mode radiation flux perturbations for imposed fields in the range  $B_0 = 0 \rightarrow 70$  (T). The plot demonstrates that with increasing departure from ideal compression (moving to the right on the  $x$  axis), magnetisation can enable the onset of the ignition. Reused with permission from Ref. [6].

and  $\rho \sim 50$  g cm $^{-3}$ , a field strength  $|\mathbf{B}| \sim 2.5$  kT is required to obtain  $\omega\tau \sim 1$  [4]. This field strength cannot be produced directly, but it is possible to produce a smaller field which, assuming frozen in magnetic field and a spherical compression, is amplified by the square of the convergence,

$$|\mathbf{B}_1| = |\mathbf{B}_0| \left( \frac{R_0}{R_1} \right)^2, \quad (1.1)$$

where  $|\mathbf{B}_0|$  and  $|\mathbf{B}_1|$  are initial and final magnetic fields respectively and  $R_0$  and  $R_1$  are initial and final radii respectively. Laboratory magnetic fields can be produced from pulsed power coils with field strength  $|\mathbf{B}| \sim \mathcal{O}(50)$  T [5], so even moderate convergence-ratio targets ( $R_0/R_1 \sim 10$ ) are able to produce strongly magnetised core plasma.

Fig. ?? plots results of magnetised indirect-drive simulations, of a target on the threshold of ignition [6]. Increasing magnitude of radiation perturbation were applied to the drive (moving to the right on the  $x$ -axis), which prevent the target from achieving ignition, which is visible as the steep increase in yield, below some threshold level of perturbation. The results demonstrate that when an initial magnetic field was applied to the target, it more robustly ignited with increasing field strength due to reduced conduction losses. This simulation work, prior to the achievement of ignition on the NIF [7], motivated the development of a magnetised ICF campaign at Lawrence Livermore National Laboratory (LLNL) [8].

The CHIMERA code has been used to study a wide array of physics relevant to magnetised ICF. Simulation work has been conducted, which has shown that magnetisation can alter instability growth of magnetised laser fusion implosions. While in the deceleration phase, magnetic tension can reduce low-mode perturbation growth [9], magnetisation of directly-driven targets inhibits heatflow in the plasma corona and thus limits thermal stabilisation of short wavelength modes from laser imprint [10]. Recent work has also demonstrated that

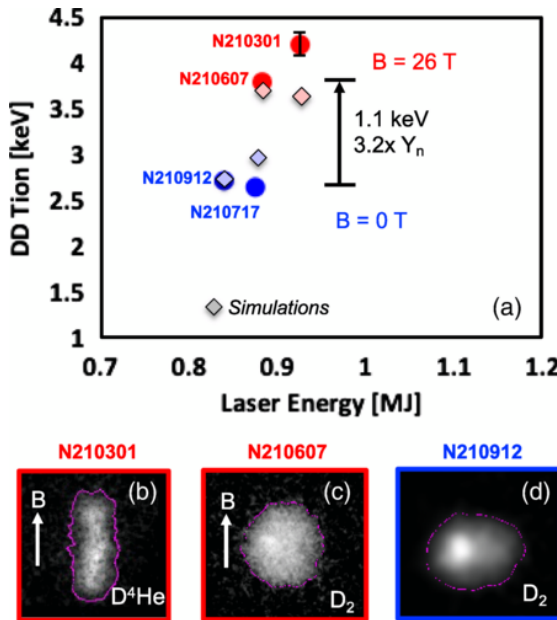


Figure 1.3: a) A 1.1 keV  $T_i$  increase was achieved by adding a 26 T  $B_0$  field to a  $D_2$  gas capsule implosion on the NIF. Also shown in the plot are the simulation results. b)–d) Equatorial shapes of the implosions. Reused with permission from Ref. [11].

magnetisation of high-yield, indirect-drive targets must be carefully optimised, in order to avoid significant degradation to the implosion shape, due to anisotropic thermal conduction and inhibition of burn propagation, due to  $\alpha$  magnetisation [4].

### 1.1.2 Experimental Studies of Magnetised-ICF

Indirect-drive experiments have been conducted on the NIF to demonstrate the efficacy of magnetised targets, in reducing thermal conduction losses in the hotspot. Non-cryogenic, deuterium filled capsules were deployed with initial field strengths up to 26 T [11]. Results from this experimental campaign are show in Fig. 1.3.a. Fig. 1.3.b, 1.3.c and 1.3.d plot x-ray images at stagnation of different experiments, showing that a shape-tuning process had to be conducted in order to optimise the sphericity of the target, due to the field leading to anisotropic thermal conduction. The magnetised targets demonstrated significantly enhanced ion temperatures and neutron yields and work is underway to explore non-uniform field configurations to further enhance the benefits of magnetisation [12].

Magnetisation of direct-drive targets has been investigated by experiments on the OMEGA laser facility for a number of years. Initial OMEGA experiments focussed on verification of magnetic flux compression, by applying an initial seed field along the axis of a cylinder that was imploded via laser irradiation [14]. The magnetised implosions validated predictions of flux compression and demonstrated enhanced neutron yields and core ion temperatures over unmagnetised implosions. Spherical targets were subsequently fielded, which also resulted in increased stagnation temperatures and yield compared to unmagnetised targets. No noticeable degradation to the implosion shape or performance was observed in these experiments, which was assumed to be due to the high ratio of plasma pressure to magnetic

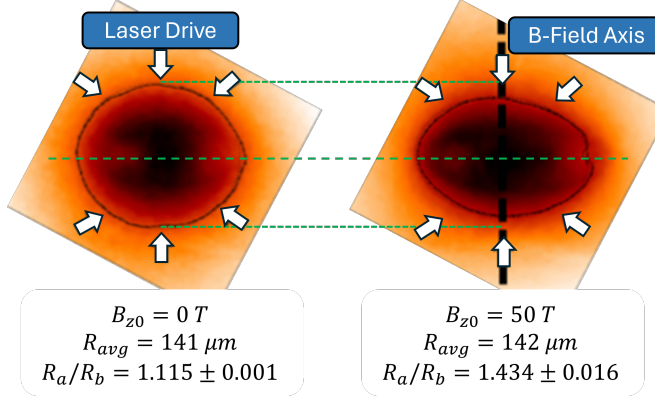


Figure 1.4: X-ray self emission images of (left) an unmagnetised and (right) a magnetised implosion. The average radius of the marked contour (corresponding to 40% of peak intensity), and the oblateness parameter  $R_a/R_b$  (ratio of major-to-minor axis) are listed below each image. The polar laser-drive is indicated by the white arrows, and the axis of the initial magnetic field by the black dashed line on the right. Applying an initial magnetic field demonstrated increased oblateness of the implosion. Adapted with permission from Ref. [13].

pressure,  $\beta \gg 1$ .

The most recent experimental, magnetised direct-drive work has focussed on exploring higher initial seed field values ( $|\mathbf{B}_0| \sim 50$  T compared to  $|\mathbf{B}_0| \sim 8$  T), to understand the saturation of performance with increasing field. A shock-driven, exploding pusher target configuration was used for these experiments, in order to create high ion temperatures and thus create a platform to study magnetised ions. Exploding pushers are significantly different implosions compared to hot-spot ignition targets discussed in previous chapters and shall be described in detail in Sec. 1.1.4. Creating these strong fields at the target necessitated reducing the radius of the equatorial field coil compared to previous experiments, and therefore a 40-beam configuration had to be used, without the 20 equatorial beams, leading to a pole heavy laser drive. The high fields of these implosions led to strongly magnetised coronal electrons,  $\omega_e \tau_e \sim 50$ , resulting in strongly anisotropic thermal conduction  $\kappa_{\perp,e}/\kappa_{\parallel,e} \sim 10^{-4}$ . This is compared to previous experiments which produced  $\omega_e \tau_e \sim 1$  and therefore  $\kappa_{\perp,e}/\kappa_{\parallel,e} \sim 1/3$ . In direct-drive on OMEGA, laser deposition is transported to the ablation surface by electron thermal conduction, thus large electron Hall parameters led to an effective asymmetry of the implosion drive.

Fig. 1.4 shows x-ray self-emission images of an unmagnetised (left) and magnetised (right) target with an initial  $|\mathbf{B}_0| = 50$  T seed field. The strongly magnetised coronal electrons led to decreased drive  $\perp \hat{\mathbf{B}_0}$ , markedly increasing the oblateness of the diagnostic image compared to the unmagnetised target. An ion magnetisation of  $\omega_i \tau_i \sim 7$  was also reported. Previous Rad-MHD modelling of these experiments, using the CHIMERA code, did not include the effects of CBET. The development of SOLAS, and particularly the CBET model, motivated further computational study of these experiments, to explore whether CBET played a significant role in dictating the shape of these implosions. This is because CBET is known to markedly compensate global,  $\ell = 1$  asymmetries [15, 16], therefore the anisotropy introduced from

magnetisation could effect the action of CBET.

### 1.1.3 Magnetised Laser-Plasma Instabilities

Some of the work conducted in this chapter, aims to understand how magnetisation of a direct drive implosion anisotropically changes the hydrodynamics, and how these altered coronal plasma conditions modify the calculated CBET gains, discussed in Sec. ???. For example, magnetisation restricts thermal conduction and therefore enhances coronal electron temperatures along the initial field axis. Approximately, the fluid CBET gain,  $\gamma_{ij} \propto T_e^{-1}$ , therefore anisotropic changes to  $T_e$  could result in reduced CBET gains around the target and therefore change CBET scattering compared to implosions without an applied field. This modification to CBET via the altered hydrodynamic profiles is called the *indirect* effect of magnetisation on LPIs.

Magnetisation can however also *directly* modify scattering from LPIs, in a number of ways. For ICF conditions, when the field strength is sufficiently high, electron cyclotron motion can become comparable to plasma wave frequencies, and therefore alter the dispersion relation of the mediating plasma wave in LPIs. In underdense, ICF relevant plasma ( $n_e \sim 10^{20} \text{ cm}^{-3}$  and  $T \sim 2 \text{ keV}$ ), the ion acoustic wave, which mediates Stimulated Brillouin Scattering (SBS) and CBET, is significantly modified when  $|\mathbf{B}| \sim 100 \text{ T}$  and the Electron Plasma Wave (EPW), which mediates acSRS and Two Plasmon Decay (TPD), when  $|\mathbf{B}| \sim 1000 \text{ T}$  [17]. Additionally, the (predominantly collisionless) damping of plasma waves can also be modified, because cyclotron motion of particles can affect their trapping in plasma waves [17]. Significant theoretical progress has been made in this field in recent years by Shi et al., who derived analytic formula for 3 wave coupling in the presence of a magnetic field [18, 19]. This was challenging due to the lack of simple geometries for the interaction, when a field is applied to a plasma with an arbitrary direction.

The simulation results here neglect this direct affect of magnetisation on CBET, partially because the theory is not yet deemed to be significantly mature, to implement within a reduced, ray-based model. Coronal magnetic field strengths of  $|\mathbf{B}| \lesssim 50 \text{ T}$  were observed in the underdense coronal plasma so significant modifications to the acoustic wave dispersion relation were not expected. It is noted however, that altered damping of the waves from magnetisation may affect the results, but the focus of the study was predominantly to explore how magnetisation might indirectly affect CBET.

### 1.1.4 The Exploding-Pusher Configuration

Exploding-pushers are considered to be a highly reproducible platform, robust to instabilities and capable of producing large neutron yields. Although historically it had a slightly different meaning [20], the term ‘exploding pusher’ is now, typically used for low convergence, thin-shell targets [21]. When irradiated with significant intensity, frequency-tripled laser light<sup>1</sup>, the thin shell rapidly heats and then explosively ablates, driving a strong shock

---

<sup>1</sup>When frequency-tripled light is not used, suprathermal electrons, rather than ablation, is the dominant driver of the strong shock [22].

radially inward, ahead of the in-falling ablated material. This shock strongly heats the ions as it propagates through gas fill to large, fusion relevant temperatures. After rebounding from the axis, the shock recompresses the infalling exploded shell material, resulting in sufficient density for a significant number of fusion reactions.

Directly-driven exploding pusher targets have the largest direct drive fusion yields recorded on the NIF, resulting in  $E_{\text{fusion}} \sim 30 \text{ kJ}$  [22]. However, they are not suitable for high gain designs, as the low areal densities of the target are not sufficient to confine  $\alpha$  particles and thus enable burn propagation. A variety of interesting physics may be studied using the platform due to the significant ion temperatures that can be achieved, such as equilibration between electrons and ions [23]. The strong shock is also highly kinetic, and thus accurate comparison to experimentally measurable variables, such as yields and ion temperatures, is expected to be difficult for Radiative-Hydrodynamics (Rad-Hydro) codes which lack a suitable model for non-local transport, such as CHIMERA. However, much of the key dynamics and results can be studied more qualitatively. !!!!!!!!!!!!!!! - Check the above sentence and get a reference - !!!!!!!!!!!!!!!

## 1.2 Cross-Beam Energy Transfer in Unmagnetised Exploding Pushers

This section presents simulation results, which demonstrate the effect of CBET in exploding pushers on OMEGA. Both 1-D and 2-D CHIMERA-SOLAS simulations of 40-beam, pole-heavy drive exploding pusher experiments are presented, with a focus on how CBET acts to change the implosion. The 1-D results demonstrate that CBET significantly reduces the coupled laser energy to the implosion from ... to .... Simulations conducted in 2-D, with a full 3-D raytrace and CBET model, clearly demonstrated that the polar drive configuration led to an oblate implosion.

### 1.2.1 Simulation Configuration

The simulations conducted for this chapter aimed to study experimental configurations similar to the results from Bose *et al.*, discussed in Sec. 1.1.2 [13]. Experimental data from these magnetised exploding pushers, demonstrated a clear amplification of the mode-2 due to magnetisation, which could affect CBET scattering. The beam configuration, capsule initial conditions and pulse shape are shown in Fig. 1.5. The exact pulse shape and target specifications were from a set of follow up experiments to Bose *et al.* and were provided by C. W. Chang and J. Frenje from Massachusetts Institute of Technology (MIT) [24]. 40 beams from the OMEGA laser, delivered a total of 17.7 kJ laser energy to a  $2.5 \mu\text{m}$  thick, glass ( $\text{SiO}_2^2$ ) capsule, filled with room temperature and pressure  $\text{D}_2$ . All experiments removed the 20 equatorial beams from the drive, because the presence of the field coil precluded them when an axial field was applied. Magnetic fields of strength  $B_{z0} = 0, 25$  and  $50 \text{ T}$  were applied along the z-axis of the configuration.

---

<sup>2</sup>By ion number density, the material was comprised of 1/3 Si and 2/3 O.

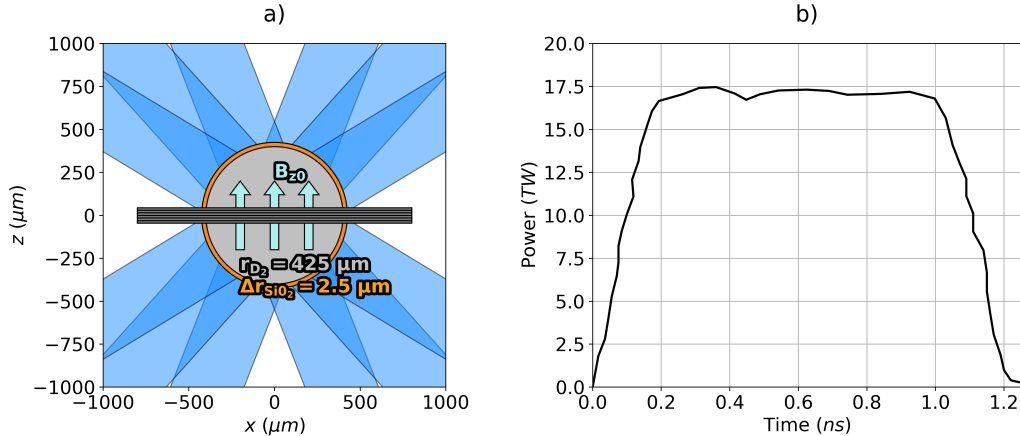


Figure 1.5: The initial conditions used for all simulations presented in this chapter. Panel a) plots the  $D_2$  filled, glass shell capsule and direction of the initial magnetic field. An example field coil (illustrative and not included in simulations) is also shown, the presence of which necessitated the polar laser drive in experiments. Panel b) plots the laser pulse shape used, which had a total of 17.7 kJ laser energy.

An explicit  $P_{1/3}$  radiation transport algorithm was used for all simulations, using tabulated opacities and emissivities from the SPK code [25]. A tabulated Sesame equation of state was used for each material [26]. The CHIMERA extended-MHD package was used, which included resistive diffusion of the magnetic field, Lorentz force of the magnetic field on the hydrodynamics, Nernst advection of the field down temperature gradients and anisotropic thermal conduction [27]. Thermal conduction was solved using a Super-time-stepping, semi-implicit algorithm [28], with flux-limited, Spitzer conductivities [29]. An electron flux limiter of  $f_{lim,e} = 0.15$  was used for all simulations. Exploding pushers exhibit high coronal temperatures due to the high- $Z$  ablator and large temperatures for the strong imploding shock, therefore simulation yields and bangtimes are highly sensitive to thermal conduction and the choice of flux limiter. Although not the focus of this work, if attempting to match simulation result to experimental yields, reducing the flux limiter value would strongly inhibit the drive and therefore reduce simulation bangtimes. In order to improve the speed of the thermal conduction algorithm, which takes small timesteps on a vacuum-plasma interface, an artificial material was placed outside the capsule, which had an enforced ionisation state of  $Z = 0$ . This had minimal impact on the implosion results, but significantly sped up simulation run-times. The presence of the material did create large viscous heating of the ions as the coronal plasma expanded into it which is visible in results throughout the chapter. However, this viscously heated layer was well separated from the region of interest (near critical) for the majority of the implosion and therefore did not impact upon the results.

All simulations used a spherical-polar CHIMERA mesh, with a fixed radial resolution of 0.5  $\mu\text{m}$ , over the full  $4\pi$  str. 1-D simulations were ran from beginning to end in spherical with  $r \in [0, 1400] \mu\text{m}$ . 2-D,  $r, \theta$  calculations assumed azimuthal symmetry of the hydrodynamics and conducted an initial ‘drive-phase’ in spherical coordinates, with  $r \in [80, 1400] \mu\text{m}$ , where the central cutout region was removed to avoid taking small radiation transport timesteps

due to the small cell faces close to the axis. The 2-D drive-phase grid used 120 cells in the polar direction. When the shock reached this cutout region, hydrodynamic variables were trilinearly interpolated onto a 2-D cylindrical  $r_{\text{cyl}}, z$  mesh with fixed resolution,  $\Delta r_{\text{cyl}} = \Delta z = 1 \mu\text{m}$ , and  $r_{\text{cyl}} \in [0, 1200] \mu\text{m}$  and  $z \in [-1200, 1200] \mu\text{m}$ , for the ‘stagnation-phase’. This grid contained no singularities, unlike a 2-D spherical grid which has no cutout, and therefore excessively small radiation transport timesteps were not an issue.

All simulations used a 3-D laser ray-trace with a variety of CBET treatments. CBET was fully included for some simulations and neglected for others. Alternatively, to explore the effect that CBET *spatial redistribution* of deposited power had on implosions, some simulations were conducted without CBET, but forced to deposit the magnitude of power that was absorbed from the equivalent CBET simulation at that time. Explicitly, these simulations conducted a no-CBET ray-trace, where the power of all rays was normalised to unity. When this raytrace was complete, it read in the absorbed power from the (previously conducted) CBET simulation at that time and multiplied the (normalised) deposited power by this value. This created a hydrodynamically similar implosion to the CBET ray-trace, and via comparison of these two simulations, the impact of CBET relocation-of-deposition upon the hydrodynamics was studied. Temporally-and-spatially integrated results from all simulations are presented in Tab. 1.1 and are referred to when relevant throughout the chapter.

### 1.2.2 1-D Simulations

### 1.2.3 2-D Simulations

## 1.3 Magnetisation in Exploding-Pusher Implosions

This section presents results of a study of the effect that extended-MHD has on the 2-D exploding pusher simulations. Simulations were conducted with varying initial magnetic field strengths and particular terms turned off and on to deduce what the important physical processes are. Magnetised transport is important for both initial seed magnetic field implosions, resulting in large coronal Hall parameters and therefore significant anisotropy of the implosions. The results demonstrate that (resistive diffusion and the Lorentz force have very little impact on the implosion physics, due to the bulk of the plasma being highly resistive and high- $\beta$  respectively)?????. The Nernst advection of magnetic field ??????????????????

Table 1.1: Results of all Simulations. In the CBET column, ‘~’ indicates CBET acted on the magnitude, but *not* spatial location, of deposition.

Run	Dim.	CBET	Note	$B_{z0}$ (T)	$t_b$ (ns)	$\langle T_i \rangle$ (keV)	$Y_n$ ( $\times 10^{10}$ )	$\Delta_b$ (ps)	$\frac{R_{\text{equator}}}{R_{\text{pole}}} \Big _{t=t_b}$
1	1-D	Off	-	0	0.69	14.66	11.62	87	$1.00^{+0.00}_{-0.00}$
2	1-D	On	-	0					$1.00^{+0.00}_{-0.00}$
3	2-D	Off	-	0	0.71	8.44	6.20	148	$2.96^{+0.20}_{-0.19}$
4	2-D	~	-	0	0.75	7.61	5.23	153	$3.26^{+0.25}_{-0.23}$
5	2-D	On	-	0	0.75	7.77	5.46	148	$3.23^{+0.25}_{-0.23}$
6	2-D	Off	-	25	0.74	7.26	4.73	130	$3.80^{+0.41}_{-0.33}$
7	2-D	~	-	25	0.78	6.58	4.14	125	$4.55^{+0.50}_{-0.43}$
8	2-D	On	-	25	0.78	6.72	4.44	123	$4.32^{+0.47}_{-0.41}$
9	2-D	Off	-	50	0.73	6.82	3.73	134	$4.40^{+0.43}_{-0.38}$
10	2-D	~	-	50	0.78	6.30	3.30	130	$4.92^{+0.56}_{-0.48}$
11	2-D	On	-	50	0.78	6.37	3.52	129	$4.79^{+0.55}_{-0.47}$
12	2-D	Off	No Aniso.	25	0.81	6.40	5.02	118	$3.14^{+0.68}_{-0.50}$
13	2-D	Off	No Lor.	25	0.74	7.29	4.77	131	$3.80^{+0.41}_{-0.33}$
14	2-D	Off	No Nern.	25	0.73	7.41	4.85	130	$3.74^{+0.38}_{-0.32}$
15	2-D	Off	No Resis.	25	0.73	7.07	4.59	132	$3.84^{+0.42}_{-0.33}$

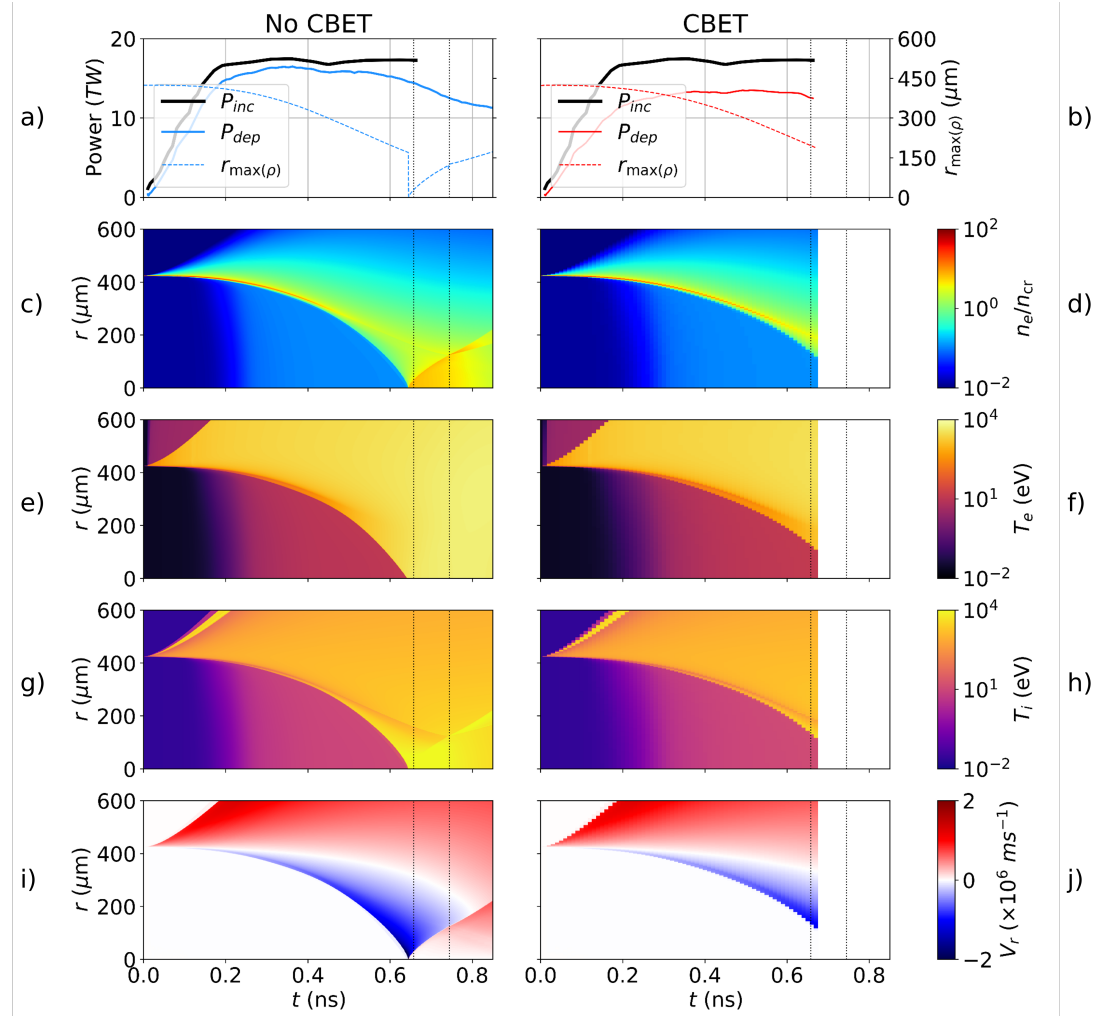


Figure 1.6: 1-D Simulation results both without (left) and with (right) CBET. The top row plots the incident and absorbed energy from the simulation on the left axis and the radius of maximum density on the right. In order, the next rows plot  $n_e$ ,  $T_e$ ,  $T_i$  and  $V_r$ . The full-width half-maximum times of the  $D_2$  yield are plotted as dotted vertical black lines on all panels.

### 1.3.1 In-Flight Field Structure

### 1.3.2 Anisotropic Thermal Conduction

### 1.3.3 The Nernst Effect

### 1.3.4 Resistive Diffusion and the Lorentz Force

## 1.4 The Effect of Magnetisation on Cross-Beam Energy Transfer and Stagnation

This section presents results on how the magnetisation of the corona affects both CBET scattering and the stagnation shape of the implosion. As was shown in the previous sections, the laser geometry leads to a significant mode  $\ell = 2$  in the coronal plasma conditions, which

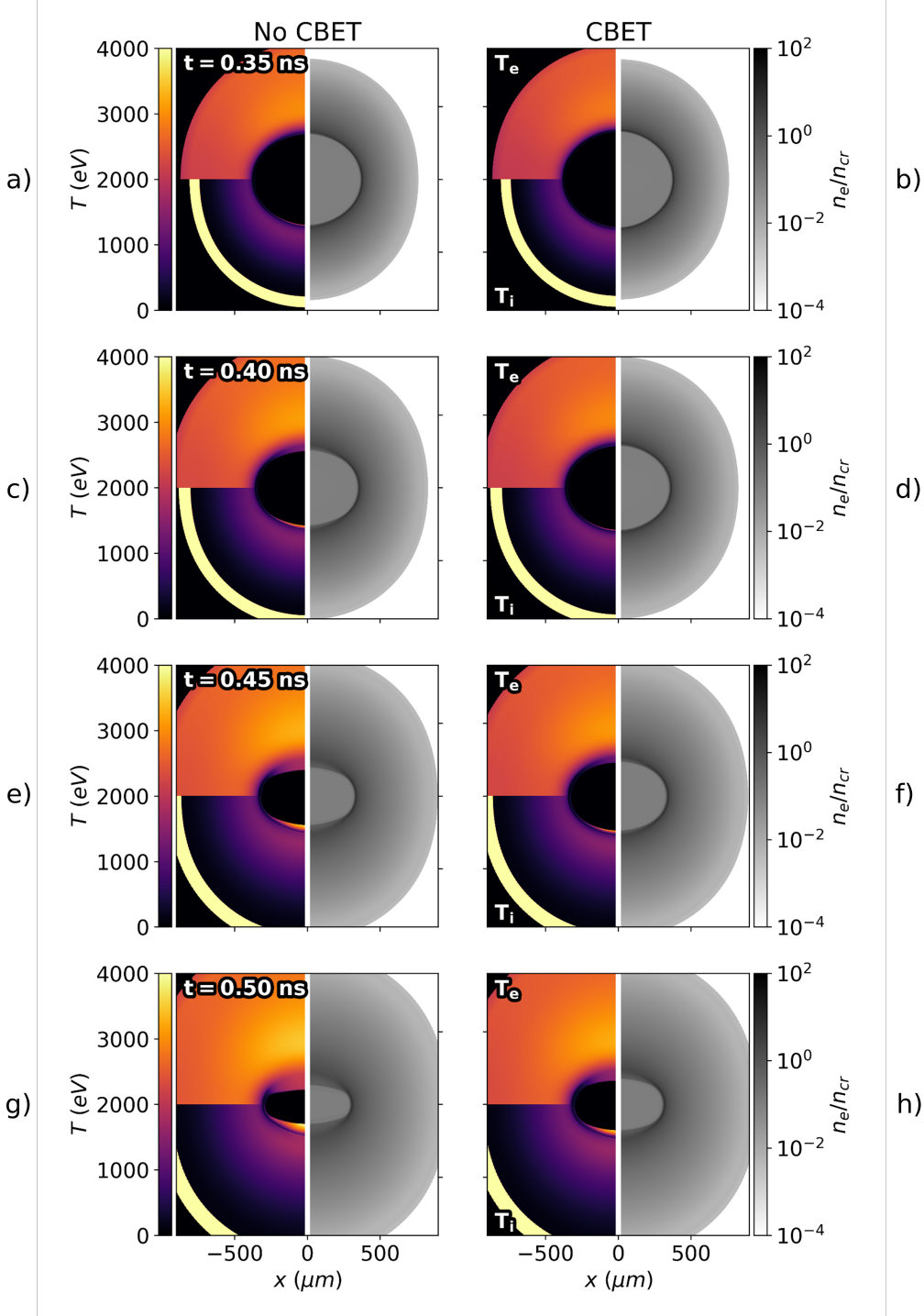


Figure 1.7:  $n_e$  (right-side),  $T_e$  (top-left-side) and  $T_i$  (bottom-left-side) plots from the 2-D, 0 T simulations without (left) and with (right) CBET at a variety of in-flight times. The decreased deposited energy due to CBET, results in lower coronal electron temperatures and therefore a slower, weaker shock being driven, which is especially evident at later times.

is significantly amplified by anisotropic thermal conduction when magnetised. This long-wavelength perturbation is slightly reduced by CBET, consistent with existing literature on how CBET mitigates  $\ell = 1$  asymmetries [16]. ‘No-CBET’ simulations were conducted, for

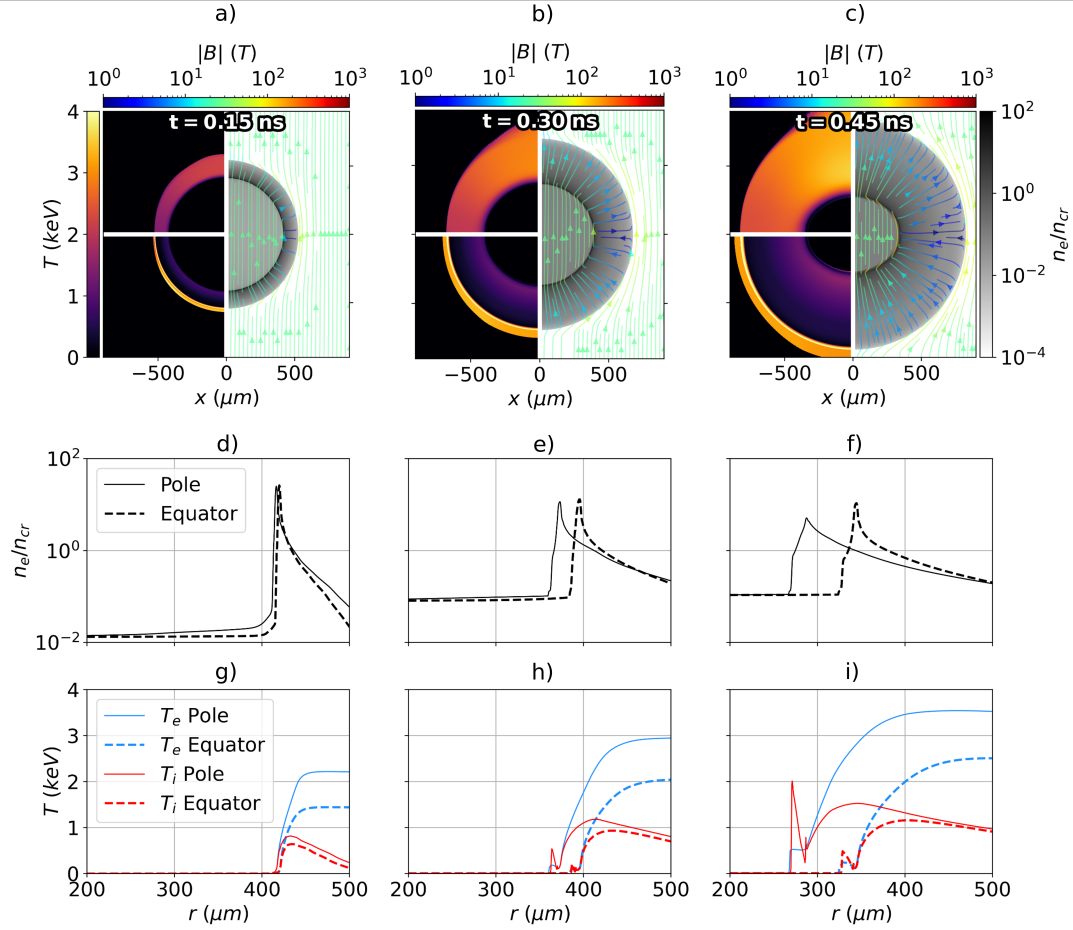


Figure 1.8: The development of the hydrodynamic variables and magnetic field structure from the  $B_{z0} = 25$  T, CBET simulation. Panels a), b) and c) plot  $T_e$  (top-left),  $T_i$  (bottom-left),  $n_e$  (right) and  $\mathbf{B}$  (streamlines) at  $t = 0.15$ ,  $0.30$  and  $0.45$  ns respectively. The approximately radially outward flowing, hot (and therefore highly conductive) ablating plasma pulls the magnetic field with it, resulting in radial  $\mathbf{B}$  field lines, which are weaker at the capsule equator. The radial field lines in the corona prevent angular equilibration of temperature, so act to keep heat at the poles. Compression of the  $\text{SiO}_2$  shell leads to a non-radial field pile up on the inside edge of the maximum density, which is most clearly visible in panel c). Panels d), e) and f) plot  $n_e$  lineouts along the pole ( $\theta = 0^\circ$ ) and equator ( $\theta = 90^\circ$ ). Panels g), h) and i) plot equivalent  $T_e$  and  $T_i$  lineouts. These all show that the increased polar temperatures, partially due to beam geometry and partially due to magnetisation, lead to preferential ablation at the pole.

which the coupled energy was kept the same as the equivalent CBET simulation, *i.e.* so CBET only acted to redistribute the deposited power, rather than reduce its magnitude. These results showed that the increasingly anisotropic coronal plasma profiles for increasing seed magnetic field strengths did lead to changes in the CBET scattering, this was too small an effect to lead to experimentally observable changes in behaviour.

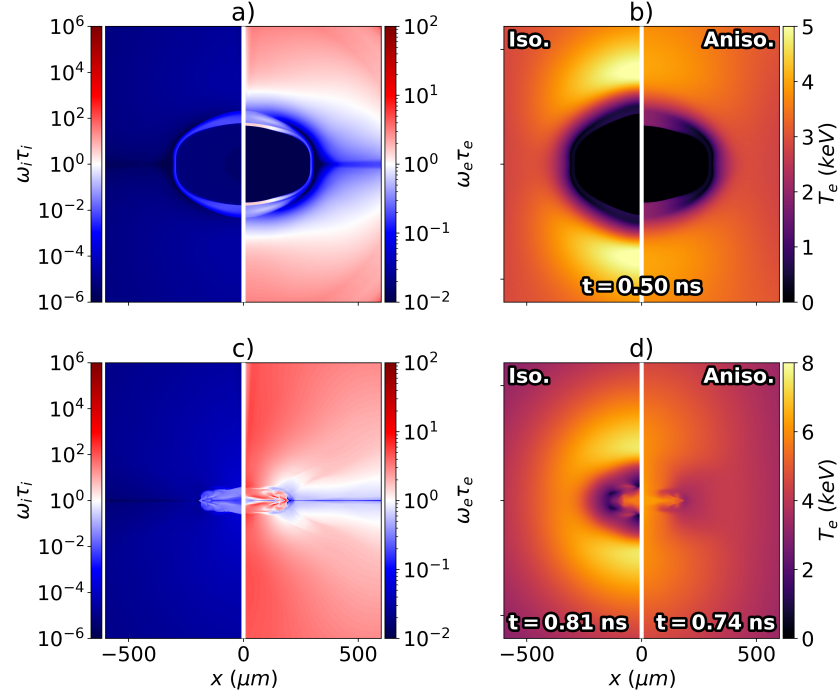


Figure 1.9: In-flight a) and bangtime c) Hall parameters, from the  $B_{z0} = 25$  T, no-CBET, anisotropic conduction simulation. Panel b) plots the  $T_e$  from the isotropically magnetised simulation (left-side) and anisotropic conduction simulation (right-side) in-flight. Panel c) plots the  $T_e$  from the isotropically magnetised simulation (left-side) and anisotropic conduction simulation (right-side) at peak neutron production. The electron Hall parameter is  $> 1$  at the poles due to high magnetic fields and temperatures, leading to significantly restricted thermal conduction from magnetised transport at the poles. Isotropically magnetised conduction (*i.e.* setting  $\kappa_{\parallel} = \kappa_{\perp}$ ), therefore results in a markedly different implosion morphology, as is shown in panels b) and d). Ion hall parameters peak at bangtime, with values reaching about  $\omega_i \tau_i \sim 0.1$ .

#### 1.4.1 Analysis and Key Definitions

#### 1.4.2 Spatial Change of CBET and Deposition from Magnetisation

#### 1.4.3 Stagnation Profiles

If CBET was anisotropically affected by magnetisation, this would result in spatial differences in deposition location, between the full CBET (top row) and CBET-on-magnitude simulations (middle row), and therefore the bangtime profiles could be different. Additionally, higher initial magnetisation increases the anisotropy of the coronal plasma and therefore

### 1.5 Conclusions

#### 1.5.1 Summary of Work

#### 1.5.2 Future Work

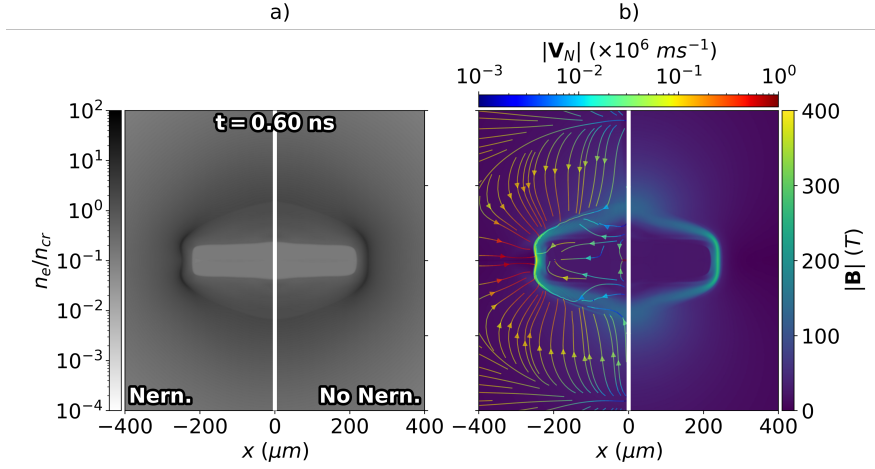


Figure 1.10: Panel a) plots in-flight electron density profiles from the  $B_{z0} = 25$  T, no-CBET simulations with (left-side) and without (right-side) Nernst advection of the magnetic field. Panel b) plots magnetic field magnitude from the Nernst (left-side) and no-Nernst (right-side) simulation. The Nernst advection velocity is also plotted for the Nernst simulation as streamlines, coloured by speed. Advection of the field is important in the low Hall parameter equatorial region, pulling  $\mathbf{B}$  down  $\nabla T_e$ , into the dense wall. Altered field at the equator impacts on the magnetised thermal conduction, which ultimately imprints on the density, as is seen in panel a).

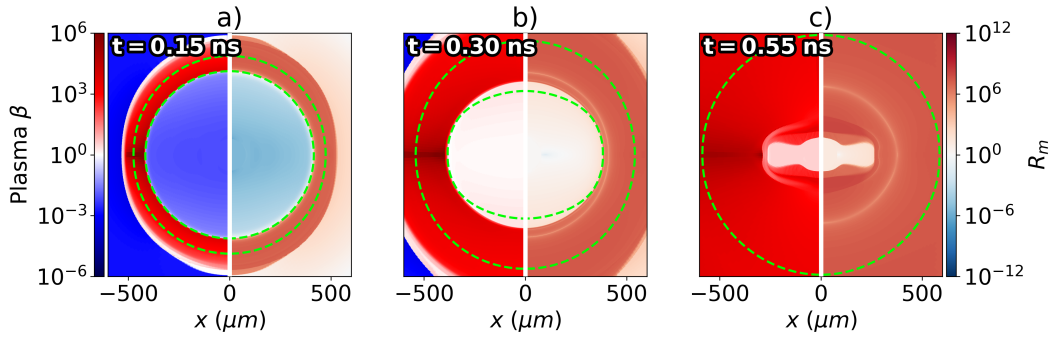


Figure 1.11: Plasma  $\beta$  (left-side) and Magnetic Reynolds Number,  $R_m$ , (right-side) at various in-flight times, throughout the  $B_{z0} = 25$  T, no-CBET simulation. Contours of the  $n_e = n_{cr}/10$  are plotted on all panels as dashed green lines to indicate the bounding region containing a significant amount plasma. Broadly, the  $\beta$  and  $R_m$  values are  $\gg 1$  in all regions with an appreciable amount of plasma, which demonstrate that the Lorentz force and resistive diffusion respectively, should have minimal effect on the implosion dynamics.

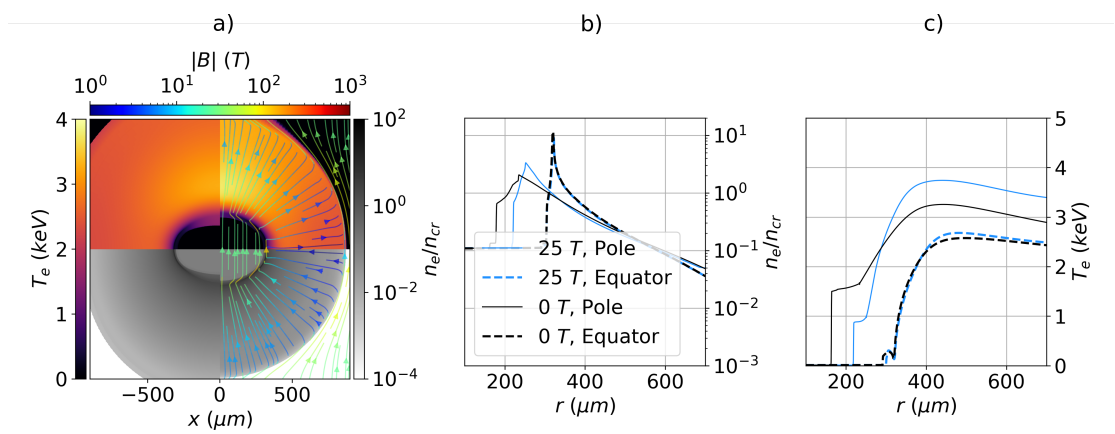


Figure 1.12: Comparison of  $n_e$  and  $T_e$  profiles from the  $B_{z0} = 0$  (panel a) left-side and 25 T (panel a) right-side, with-CBET simulations, both at  $t = 0.5$  ns. Panel a) also plots streamlines of  $\mathbf{B}$  for the  $B_{z0} = 25$  T simulation, coloured by the field magnitude. Panels b) and c) plot  $n_e$  and  $T_e$  lineouts respectively, along both the pole and equator. It is evident from these lineouts that magnetisation anisotropically affects hydrodynamic variables, which are used to calculate the CBET gain. Therefore, it is anticipated that magnetisation could anisotropically affect the CBET scattering volume.

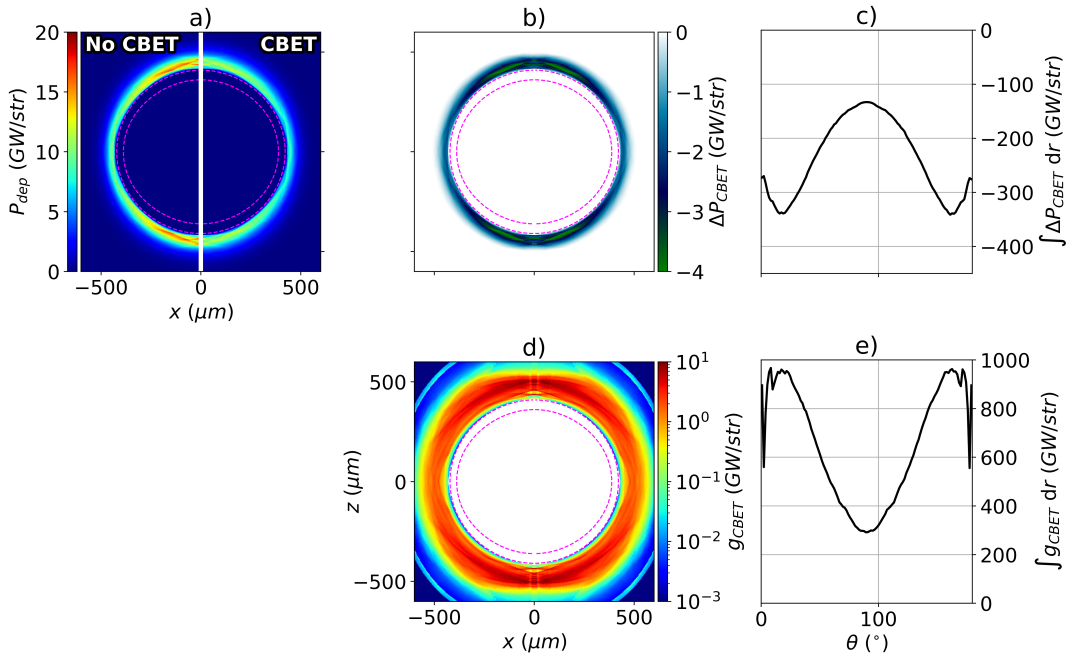


Figure 1.13: Various CBET diagnostics used in the analysis presented in this section. All plots are from the  $B_{z0} = 0$  T, with-CBET simulation at  $t = 0.30$  ns. Panel a) plots the instantaneous deposition with (right-side) and without (left-side) the effect of CBET. The ‘CBET-deficit’,  $\Delta P_{CBET}$ , which is the no-CBET deposition, subtracted from the with-CBET deposition, is plotted in panel b). Panel c) plots the radially integrated  $\Delta P_{CBET}$ , as a function of polar angle. The ‘CBET-scattering’, defined in Eq. ??, is plotted in panel d), and the radial integral is plotted in panel e). At this time, it is evident from panel e) that more CBET occurs at the capsule poles, resulting in a CBET-reduction of deposition near the poles, seen in panel c).

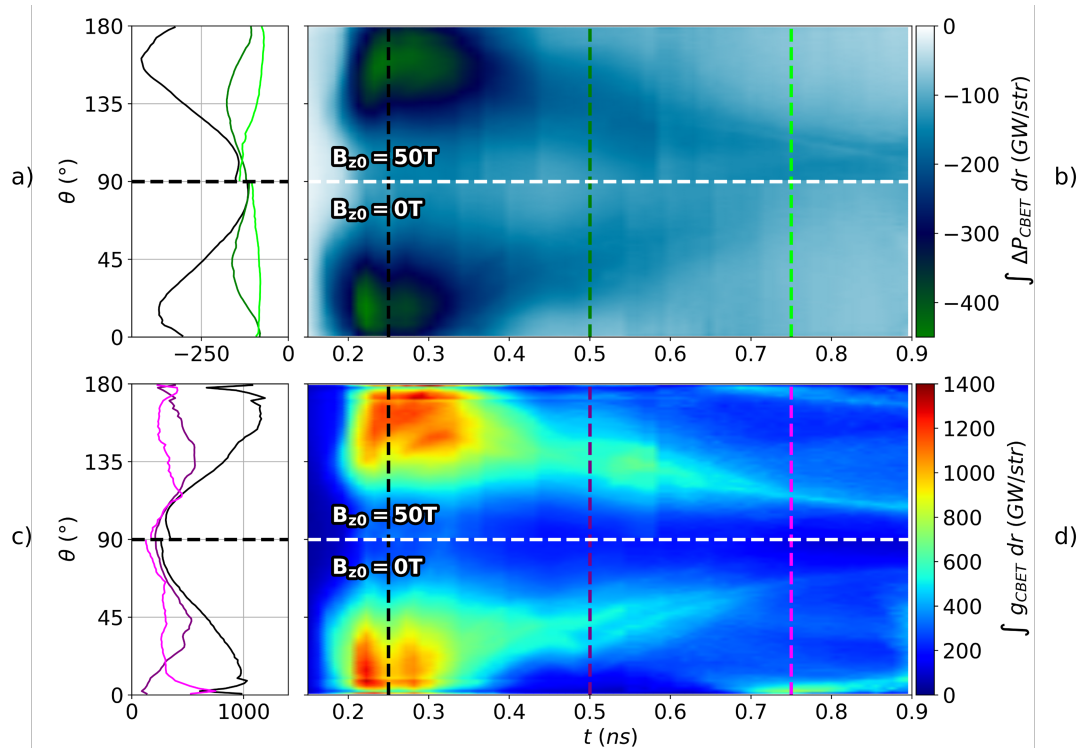


Figure 1.14: The radially integrated CBET-deficit and CBET-scattering, plotted as a function of angle and time for the  $B_{z0} = 0$  and 50 T, with-CBET simulations. Panel b) plots the CBET-deficit from the 50 T (top-half) and 0 T (bottom-half) simulations. Lineouts in  $\theta$  at  $t = 0.25$  (black), 0.50 (dark-green) and 0.75 ns (light-green) are plotted in panel a). The same results, but for CBET-scattering are plotted in panels d) and c). It is evident from these plots that for both simulations, as time progresses and the poles of the capsule fall in faster than the equator, the region where CBET mostly occurs, shifts in angle around the capsule. Differences are visible in all plots between the  $B_{z0} = 0$  and 50 T simulations, indicating that magnetisation affected CBET indirectly, via the altered hydrodynamics.

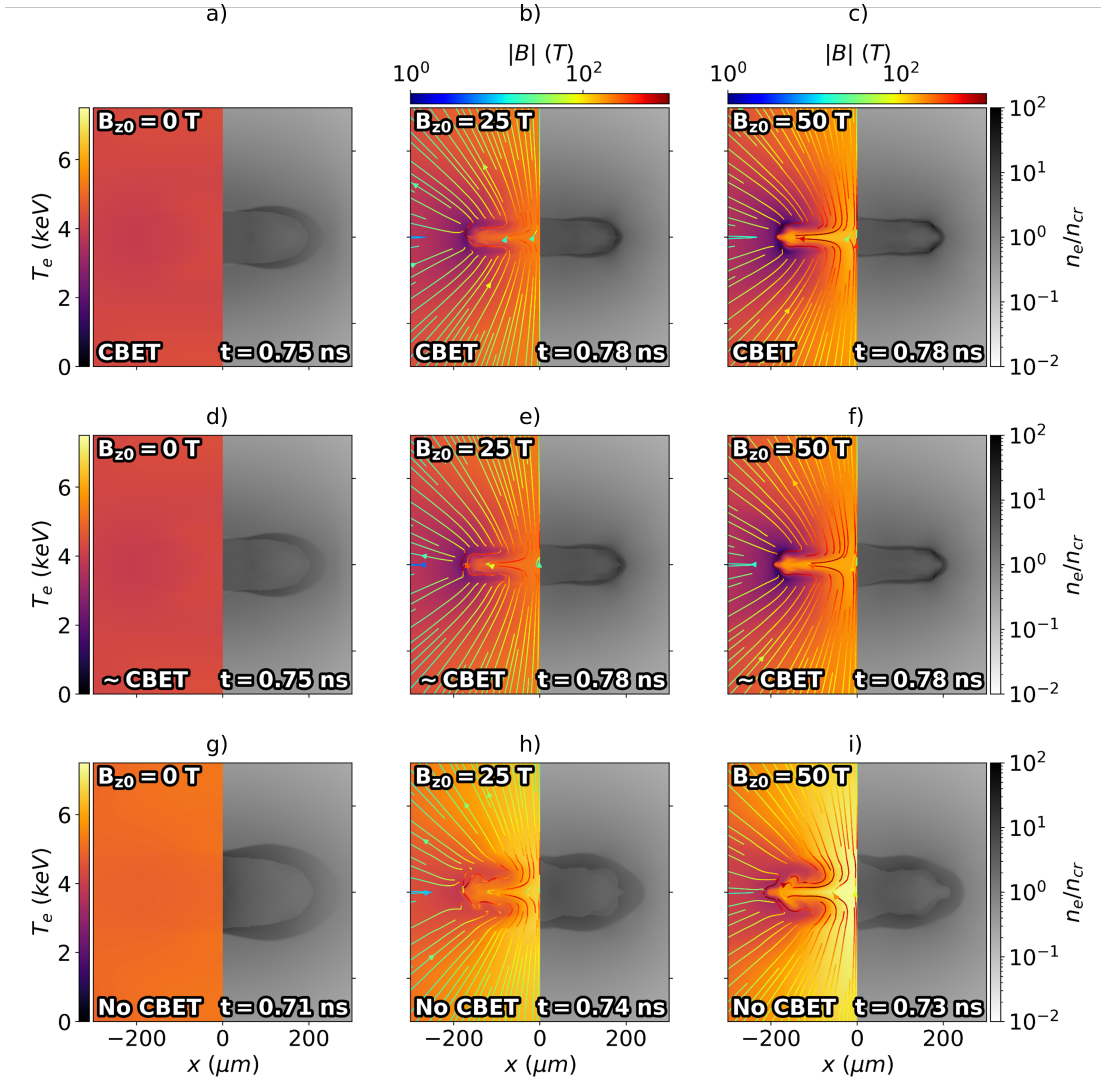


Figure 1.15:  $n_e$ ,  $T_e$  and  $\mathbf{B}$  profiles from the time of peak neutron production for different initial magnetisation (columns) and CBET effects (rows). Panels a), b) and c) are from the full CBET simulations, which show that magnetisation increases the oblateness of the stagnation profile. Panels d), e) and f) are from the simulations where only the CBET effect on the magnitude, but not spatial location, of deposition was included. These simulations have identical coupled energy to the top row, and therefore have the same bangtimes. Panels g), h) and i) are from the no-CBET simulations, which have earlier bangtimes and increased temperatures due to the higher coupled energy.

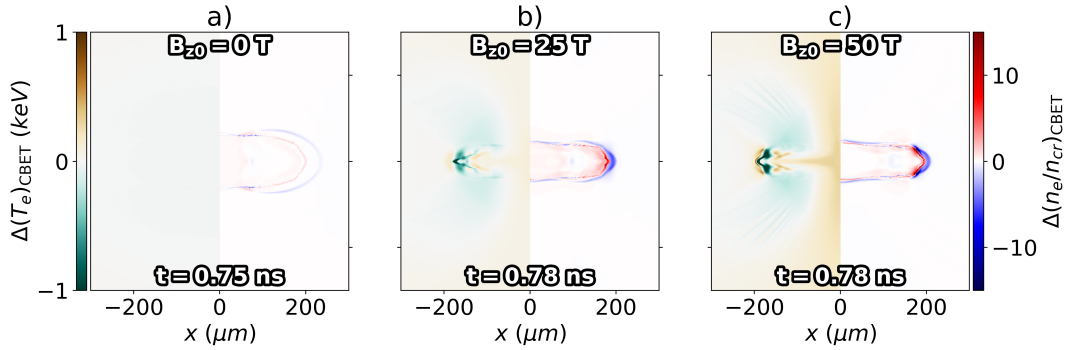


Figure 1.16: Difference in  $n_e$  and  $T_e$  bangtime profiles, between the full-CBET and CBET-magnitude a)  $B_{z0} = 0$  T, b)  $B_{z0} = 25$  T and c)  $B_{z0} = 50$  T simulations. The difference in variable  $\nu$ ,  $\Delta\nu$  is the  $\nu_{full-CB} - \nu_{magCB}$ , so higher colour scale values represent regions with increased  $\nu$  for the full CBET calculation. These results primarily show that CBET slightly reduces the bangtime equatorial radius, and thus reduces the oblateness, compared to simulations where the spatial redistribution of power due to CBET is neglected.

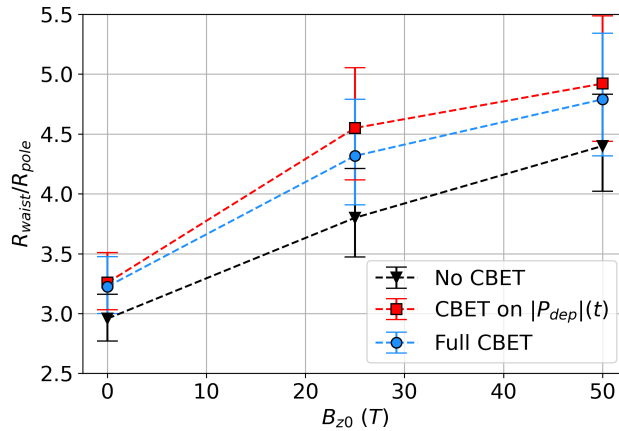


Figure 1.17: The oblateness of bangtime density profiles for different magnetisation and CBET effects. All values and errors were obtained by fitting an ellipse (with axes orientated along  $\hat{x}$  and  $\hat{z}$ ), to the radius of maximum density. No-CBET simulations are consistently more round, because the initial shock is stronger and therefore travels ahead of the pusher material more quickly than the CBET equivalent. Thus, after rebounding off the axis, it meets the infalling mass and produces thermonuclear conditions at a larger radius. As was seen in Fig. 1.16, throughout the entire implosion, when including the effect of CBET on spatial location of deposition, it acts to slightly move energy from the pole to the waist and thus marginally reduces oblateness of the implosion.

## **Appendices**



# Bibliography

- [1] I.R. Lindemuth and R.C. Kirkpatrick. Parameter space for magnetized fuel targets in inertial confinement fusion. *Nuclear Fusion*, 23(3):263–284, March 1983. ISSN 0029-5515, 1741-4326. doi: 10.1088/0029-5515/23/3/001. URL <https://iopscience.iop.org/article/10.1088/0029-5515/23/3/001>. 6
- [2] R.D. Jones and W.C. Mead. The physics of burn in magnetized deuterium-tritium plasmas: spherical geometry. *Nuclear Fusion*, 26(2):127–137, February 1986. ISSN 0029-5515, 1741-4326. doi: 10.1088/0029-5515/26/2/001. URL <https://iopscience.iop.org/article/10.1088/0029-5515/26/2/001>. 6
- [3] E. M. Epperlein and M. G. Haines. Plasma transport coefficients in a magnetic field by direct numerical solution of the Fokker-Planck equation. *The Physics of Fluids*, 29(4):1029–1041, April 1986. ISSN 0031-9171. doi: 10.1063/1.865901. URL <https://pubs.aip.org/pfl/article/29/4/1029/819331/Plasma-transport-coefficients-in-a-magnetic-field>. 6
- [4] Sam Thomas Jack O'Neill. *Modelling Ignition and Burn in Pre-magnetised Inertial Confinement Fusion Experiments*. PhD thesis, Imperial College London, London, December 2023. 7, 8
- [5] G. Fiksel, A. Agliata, D. Barnak, G. Brent, P.-Y. Chang, L. Folnsbee, G. Gates, D. Hasset, D. Lonobile, J. Magoon, D. Mastrosimone, M. J. Shoup, and R. Betti. Note: Experimental platform for magnetized high-energy-density plasma studies at the omega laser facility. *Review of Scientific Instruments*, 86(1):016105, January 2015. ISSN 0034-6748, 1089-7623. doi: 10.1063/1.4905625. URL <https://pubs.aip.org/rsi/article/86/1/016105/360963>Note-Experimental-platform-for-magnetized-high>. 7
- [6] L. J. Perkins, D. D.-M Ho, B. G. Logan, G. B. Zimmerman, M. A. Rhodes, D. J. Strozzi, D. T. Blackfield, and S. A. Hawkins. The potential of imposed magnetic fields for enhancing ignition probability and fusion energy yield in indirect-drive inertial confinement fusion. *Physics of Plasmas*, 24(6):062708, June 2017. ISSN 1070-664X, 1089-7674. doi: 10.1063/1.4985150. URL <https://pubs.aip.org/pop/article/24/6/062708/108192/The-potential-of-imposed-magnetic-fields-for>. 7
- [7] A. B. Zylstra, O. A. Hurricane, D. A. Callahan, A. L. Kritcher, J. E. Ralph, H. F. Robey, J. S. Ross, C. V. Young, K. L. Baker, D. T. Casey, T. Döppner, L. Divol, M. Hohenberger, S. Le Pape, A. Pak, P. K. Patel, R. Tommasini, S. J. Ali, P. A. Amendt, L. J. Atherton, B. Bachmann, D. Bailey, L. R. Benedetti, L. Berzak Hopkins, R. Betti, S. D. Bhandarkar,

- J. Biener, R. M. Bionta, N. W. Birge, E. J. Bond, D. K. Bradley, T. Braun, T. M. Briggs, M. W. Bruhn, P. M. Celliers, B. Chang, T. Chapman, H. Chen, C. Choate, A. R. Christoperson, D. S. Clark, J. W. Crippen, E. L. Dewald, T. R. Dittrich, M. J. Edwards, W. A. Farmer, J. E. Field, D. Fittinghoff, J. Frenje, J. Gaffney, M. Gatu Johnson, S. H. Glenzer, G. P. Grim, S. Haan, K. D. Hahn, G. N. Hall, B. A. Hammel, J. Harte, E. Hartouni, J. E. Heebner, V. J. Hernandez, H. Herrmann, M. C. Herrmann, D. E. Hinkel, D. D. Ho, J. P. Holder, W. W. Hsing, H. Huang, K. D. Humbird, N. Izumi, L. C. Jarrott, J. Jeet, O. Jones, G. D. Kerbel, S. M. Kerr, S. F. Khan, J. Kilkenny, Y. Kim, H. Geppert Kleinrath, V. Geppert Kleinrath, C. Kong, J. M. Koning, J. J. Kroll, M. K. G. Kruse, B. Kustowski, O. L. Landen, S. Langer, D. Larson, N. C. Lemos, J. D. Lindl, T. Ma, M. J. MacDonald, B. J. MacGowan, A. J. Mackinnon, S. A. McLaren, A. G. MacPhee, M. M. Marinak, D. A. Mariscal, E. V. Marley, L. Masse, K. Meaney, N. B. Meezan, P. A. Michel, M. Millot, J. L. Milovich, J. D. Moody, A. S. Moore, J. W. Morton, T. Murphy, K. Newman, J.-M. G. Di Nicola, A. Nikroo, R. Nora, M. V. Patel, L. J. Pelz, J. L. Peterson, Y. Ping, B. B. Pollock, M. Ratledge, N. G. Rice, H. Rinderknecht, M. Rosen, M. S. Rubery, J. D. Salmonson, J. Sater, S. Schiaffino, D. J. Schlossberg, M. B. Schneider, C. R. Schroeder, H. A. Scott, S. M. Sepke, K. Sequoia, M. W. Sherlock, S. Shin, V. A. Smalyuk, B. K. Spears, P. T. Springer, M. Stadermann, S. Stoupin, D. J. Strozzi, L. J. Suter, C. A. Thomas, R. P. J. Town, E. R. Tubman, C. Trosseille, P. L. Volegov, C. R. Weber, K. Widmann, C. Wild, C. H. Wilde, B. M. Van Wonterghem, D. T. Woods, B. N. Woodworth, M. Yamaguchi, S. T. Yang, and G. B. Zimmerman. Burning plasma achieved in inertial fusion. *Nature*, 601(7894):542–548, January 2022. ISSN 1476-4687. doi: 10.1038/s41586-021-04281-w. URL <https://www.nature.com/articles/s41586-021-04281-w>. Publisher: Nature Publishing Group. 7
- [8] J. D. Moody, B. B. Pollock, H. Sio, D. J. Strozzi, D. D.-M. Ho, C. Walsh, G. E. Kemp, S. O. Kucheyev, B. Kozioziemski, E. G. Carroll, J. Kroll, D. K. Yanagisawa, J. Angus, S. D. Bhandarkar, J. D. Bude, L. Divol, B. Ferguson, J. Fry, L. Hagler, E. Hartouni, M. C. Herrmann, W. Hsing, D. M. Holunga, J. Javedani, A. Johnson, D. Kalantar, T. Kohut, B. G. Logan, N. Masters, A. Nikroo, N. Orsi, K. Piston, C. Provencher, A. Rowe, J. Sater, K. Skulina, W. A. Stygar, V. Tang, S. E. Winters, J. P. Chittenden, B. Appelbe, A. Boxall, A. Crilly, S. O'Neill, J. Davies, J. Peebles, and S. Fujioka. The Magnetized Indirect Drive Project on the National Ignition Facility. *Journal of Fusion Energy*, 41(1): 7, June 2022. ISSN 0164-0313, 1572-9591. doi: 10.1007/s10894-022-00319-7. URL <https://link.springer.com/10.1007/s10894-022-00319-7>. 7
- [9] C. A. Walsh, K. McGlinchey, J. K. Tong, B. D. Appelbe, A. Crilly, M. F. Zhang, and J. P. Chittenden. Perturbation modifications by pre-magnetisation of inertial confinement fusion implosions. *Physics of Plasmas*, 26(2):022701, February 2019. ISSN 1070-664X, 1089-7674. doi: 10.1063/1.5085498. URL <https://pubs.aip.org/pop/article/26/2/022701/253631/Perturbation-modifications-by-pre-magnetisation-of>. 7
- [10] C.A. Walsh, A.J. Crilly, and J.P. Chittenden. Magnetized directly-driven ICF capsules:

- increased instability growth from non-uniform laser drive. *Nuclear Fusion*, 60(10):106006, October 2020. ISSN 0029-5515, 1741-4326. doi: 10.1088/1741-4326/abab52. URL <https://iopscience.iop.org/article/10.1088/1741-4326/abab52>. 7
- [11] J. D. Moody, B. B. Pollock, H. Sio, D. J. Strozzi, D. D.-M. Ho, C. A. Walsh, G. E. Kemp, B. Lahmann, S. O. Kucheyev, B. Kozioziemski, E. G. Carroll, J. Kroll, D. K. Yanagisawa, J. Angus, B. Bachmann, S. D. Bhandarkar, J. D. Bude, L. Divol, B. Ferguson, J. Fry, L. Haugler, E. Hartouni, M. C. Herrmann, W. Hsing, D. M. Holunga, N. Izumi, J. Javedani, A. Johnson, S. Khan, D. Kalantar, T. Kohut, B. G. Logan, N. Masters, A. Nikroo, N. Orsi, K. Piston, C. Provencher, A. Rowe, J. Sater, K. Skulina, W. A. Stygar, V. Tang, S. E. Winters, G. Zimmerman, P. Adrian, J. P. Chittenden, B. Appelbe, A. Boxall, A. Crilly, S. O'Neill, J. Davies, J. Peebles, and S. Fujioka. Increased Ion Temperature and Neutron Yield Observed in Magnetized Indirectly Driven D<sub>2</sub>-Filled Capsule Implosions on the National Ignition Facility. *Physical Review Letters*, 129(19):195002, November 2022. ISSN 0031-9007, 1079-7114. doi: 10.1103/PhysRevLett.129.195002. URL <https://link.aps.org/doi/10.1103/PhysRevLett.129.195002>. 8
- [12] Chris Walsh, Dave Strozzi, John Moody, Hong Sio, Bradley Pollock, Brandon Lahmann, Blagoje Djordjevic, Alexander Lumbard, Alexander Povilus, Jeremy Chittenden, Sam O'Neill, Aidan Crilly, and Brian Appelbe. Application of Non-Uniform Magnetic Fields to Inertial Confinement Fusion Implosions. 2023:JO07.014, January 2023. URL <https://ui.adsabs.harvard.edu/abs/2023APS..DPPJ07014W>. Conference Name: APS Division of Plasma Physics Meeting Abstracts ADS Bibcode: 2023APS..DPPJ07014W. 8
- [13] A. Bose, J. Peebles, C. A. Walsh, J. A. Frenje, N. V. Kabadi, P. J. Adrian, G. D. Sutcliffe, M. Gatū Johnson, C. A. Frank, J. R. Davies, R. Betti, V. Yu. Glebov, F. J. Marshall, S. P. Regan, C. Stoeckl, E. M. Campbell, H. Sio, J. Moody, A. Crilly, B. D. Appelbe, J. P. Chittenden, S. Atzeni, F. Barbato, A. Forte, C. K. Li, F. H. Séguin, and R. D. Petrasso. Effect of Strongly Magnetized Electrons and Ions on Heat Flow and Symmetry of Inertial Fusion Implosions. *Physical Review Letters*, 128(19):195002, May 2022. ISSN 0031-9007, 1079-7114. doi: 10.1103/PhysRevLett.128.195002. URL <https://link.aps.org/doi/10.1103/PhysRevLett.128.195002>. 9, 11
- [14] O. V. Gotchev, P. Y. Chang, J. P. Knauer, D. D. Meyerhofer, O. Polomarov, J. Frenje, C. K. Li, M. J.-E. Manuel, R. D. Petrasso, J. R. Rygg, F. H. Séguin, and R. Betti. Laser-Driven Magnetic-Flux Compression in High-Energy-Density Plasmas. *Physical Review Letters*, 103(21):215004, November 2009. ISSN 0031-9007, 1079-7114. doi: 10.1103/PhysRevLett.103.215004. URL <https://link.aps.org/doi/10.1103/PhysRevLett.103.215004>. 8
- [15] K. S. Anderson, C. J. Forrest, O. M. Mannion, F. J. Marshall, R. C. Shah, D. T. Michel, J. A. Marozas, P. B. Radha, D. H. Edgell, R. Epstein, V. N. Goncharov, J. P. Knauer, M. Gatū Johnson, and S. Laffite. Effect of cross-beam energy transfer on target-offset asymmetry in direct-drive inertial confinement fusion implosions.

- Physics of Plasmas*, 27(11):112713, November 2020. ISSN 1070-664X, 1089-7674. doi: 10.1063/5.0015781. URL <https://pubs.aip.org/pop/article/27/11/112713/107948/Effect-of-cross-beam-energy-transfer-on-target>. 9
- [16] A. Colaïtis, I. Igumenshchev, J. Mathiaud, and V. Goncharov. Inverse ray tracing on icosahedral tetrahedron grids for non-linear laser plasma interaction coupled to 3D radiation hydrodynamics. *Journal of Computational Physics*, 443:110537, October 2021. ISSN 0021-9991. doi: 10.1016/j.jcp.2021.110537. URL <https://www.sciencedirect.com/science/article/pii/S0021999121004320>. 9, 16
- [17] Yuan Shi. Benchmarking magnetised three-wave coupling for laser backscattering: analytic solutions and kinetic simulations. *Journal of Plasma Physics*, 89(3):905890305, June 2023. ISSN 0022-3778, 1469-7807. doi: 10.1017/S0022377823000405. URL [https://www.cambridge.org/core/product/identifier/S0022377823000405/type/journal\\_article](https://www.cambridge.org/core/product/identifier/S0022377823000405/type/journal_article). 10
- [18] Yuan Shi, Hong Qin, and Nathaniel J. Fisch. Three-wave scattering in magnetized plasmas: From cold fluid to quantized Lagrangian. *Physical Review E*, 96(2):023204, August 2017. ISSN 2470-0045, 2470-0053. doi: 10.1103/PhysRevE.96.023204. URL <https://link.aps.org/doi/10.1103/PhysRevE.96.023204>. 10
- [19] Yuan Shi, Hong Qin, and Nathaniel J. Fisch. Laser-plasma interactions in magnetized environment. *Physics of Plasmas*, 25(5):055706, May 2018. ISSN 1070-664X, 1089-7674. doi: 10.1063/1.5017980. URL <https://pubs.aip.org/pop/article/25/5/055706/1061011/Laser-plasma-interactions-in-magnetized>. 10
- [20] R. S. Craxton, K. S. Anderson, T. R. Boehly, V. N. Goncharov, D. R. Harding, J. P. Knauer, R. L. McCrory, P. W. McKenty, D. D. Meyerhofer, J. F. Myatt, A. J. Schmitt, J. D. Sethian, R. W. Short, S. Skupsky, W. Theobald, W. L. Kruer, K. Tanaka, R. Betti, T. J. B. Collins, J. A. Delettrez, S. X. Hu, J. A. Marozas, A. V. Maximov, D. T. Michel, P. B. Radha, S. P. Regan, T. C. Sangster, W. Seka, A. A. Solodov, J. M. Soures, C. Stoeckl, and J. D. Zuegel. Direct-drive inertial confinement fusion: A review. *Physics of Plasmas*, 22(11):110501, November 2015. ISSN 1070-664X, 1089-7674. doi: 10.1063/1.4934714. URL <https://pubs.aip.org/pop/article/22/11/110501/109006/Direct-drive-inertial-confinement-fusion-A-review>. 10
- [21] C. Leland Ellison, Heather D. Whitley, Colin R. D. Brown, Sean R. Copeland, Warren J. Garbett, Hai P. Le, Marilyn B. Schneider, Zachary B. Walters, Hui Chen, John I. Castor, R. Stephen Craxton, Maria Gatu Johnson, Emma M. Garcia, Frank R. Graziani, G. Elijah Kemp, Christine M. Krauland, Patrick W. McKenty, Brandon Lahmann, Jesse E. Pino, Michael S. Rubery, Howard A. Scott, Ronnie Shepherd, and Hong Sio. Development and modeling of a polar-direct-drive exploding pusher platform at the National Ignition Facility. *Physics of Plasmas*, 25(7):072710, July 2018. ISSN 1070-664X, 1089-7674. doi: 10.1063/1.5025724. URL <https://pubs.aip.org/pop/article/25/7/072710/319433/Development-and-modeling-of-a-polar-direct-drive>. 10

- [22] C.B. Yeamans, G.E. Kemp, Z.B. Walters, H.D. Whitley, P.W. McKenty, E.M. Garcia, Y. Yang, R.S. Craxton, and B.E. Blue. High yield polar direct drive fusion neutron sources at the National Ignition Facility. *Nuclear Fusion*, 61(4):046031, April 2021. ISSN 0029-5515, 1741-4326. doi: 10.1088/1741-4326/abe4e6. URL <https://iopscience.iop.org/article/10.1088/1741-4326/abe4e6>. 10, 11
- [23] Lorin X. Benedict, Michael P. Surh, John I. Castor, Saad A. Khairallah, Heather D. Whitley, David F. Richards, James N. Glosli, Michael S. Murillo, Christian R. Scullard, Paul E. Grabowski, David Michta, and Frank R. Graziani. Molecular dynamics simulations and generalized Lenard-Balescu calculations of electron-ion temperature equilibration in plasmas. *Physical Review E*, 86(4):046406, October 2012. ISSN 1539-3755, 1550-2376. doi: 10.1103/PhysRevE.86.046406. URL <https://link.aps.org/doi/10.1103/PhysRevE.86.046406>. 11
- [24] Cody Wu Chang and J. A. Frenje, April 2023. 11
- [25] A.J. Crilly, N.P.L. Niasse, A.R. Fraser, D.A. Chapman, K.W. McLean, S.J. Rose, and J.P. Chittenden. SpK: A fast atomic and microphysics code for the high-energy-density regime. *High Energy Density Physics*, 48:101053, September 2023. ISSN 15741818. doi: 10.1016/j.hedp.2023.101053. URL <https://linkinghub.elsevier.com/retrieve/pii/S1574181823000198>. 12
- [26] James McHardy. An introduction to the theory and use of SESAME equations of state. Technical Report LA-14503, 1487368, December 2018. URL <https://www.osti.gov/servlets/purl/1487368/>. 12
- [27] C. A. Walsh, J. P. Chittenden, D. W. Hill, and C. Ridgers. Extended-magnetohydrodynamics in under-dense plasmas. *Physics of Plasmas*, 27(2):022103, February 2020. ISSN 1070-664X, 1089-7674. doi: 10.1063/1.5124144. URL <https://pubs.aip.org/pop/article/27/2/022103/841709/Extended-magnetohydrodynamics-in-under-dense>. 12
- [28] Bhargav Vaidya, Deovrat Prasad, Andrea Mignone, Prateek Sharma, and Luca Rickler. Scalable explicit implementation of anisotropic diffusion with Runge–Kutta–Legendre super-time stepping. *Monthly Notices of the Royal Astronomical Society*, 472(3):3147–3160, December 2017. ISSN 0035-8711, 1365-2966. doi: 10.1093/mnras/stx2176. URL <http://academic.oup.com/mnras/article/472/3/3147/4093858/Scalable-explicit-implementation-of-anisotropic>. 12
- [29] Lyman Spitzer and Richard Härm. Transport Phenomena in a Completely Ionized Gas. *Physical Review*, 89(5):977–981, March 1953. ISSN 0031-899X. doi: 10.1103/PhysRev.89.977. URL <https://link.aps.org/doi/10.1103/PhysRev.89.977>. 12



## **Permissions**